Geophysical Research Letters

RESEARCH LETTER
10.1029/2018GL081135

Geodetic Evidence That Mercury Has A Solid Inner Core

Antonio Genova[1,2,3], Sander Goossens[2,4], Erwan Mazarico[2], Frank G. Lemoine[2], Gregory A. Neumann[2], Weijia Kuang[2], Terence J. Sabaka[2], Steven A. Hauck II[5], David E. Smith[1], Sean C. Solomon[6], and Maria T. Zuber[1]

[1]Department of Earth, Atmospheric and Planetary Sciences, Massachusetts Institute of Technology, Cambridge, MA, USA, [2]NASA Goddard Space Flight Center, Greenbelt, MD, USA, [3]Department of Mechanical and Aerospace Engineering, Sapienza Univesity of Rome, Rome, Italy, [4]Center for Research and Exploration in Space Science and Technology, University of Maryland, Baltimore County, Baltimore, MD, USA, [5]Department of Earth, Environmental, and Planetary Sciences, Case Western Reserve University, Cleveland, OH, USA, [6]Lamont-Doherty Earth Observatory, Columbia University, Palisades, NY, USA

Abstract Geodetic analysis of radio tracking measurements of the MErcury Surface, Space ENvironment, GEochemistry, and Ranging spacecraft while in orbit about Mercury has yielded new estimates for the planet's gravity field, tidal Love number, and pole coordinates. The derived right ascension ($\alpha = 281.0082° \pm 0.0009°$; all uncertainties are 3 standard deviations) and declination ($\delta = 61.4164° \pm 0.0003°$) of the spin pole place Mercury in the Cassini state. Confirmation of the equilibrium state with an estimated mean (whole planet) obliquity ϵ of 1.968 ± 0.027 arcmin enables the confident determination of the planet's normalized polar moment of inertia (0.333 ± 0.005), which indicates a high degree of internal differentiation. Internal structure models generated by a Markov Chain Monte Carlo process and consistent with the geodetic constraints possess a solid inner core with a radius (r_{ic}) between 0.3 and 0.7 that of the outer core (r_{oc}).

Key Points:
- New solution for Mercury's gravity field provides crucial information on the planet's tidal response and orientation
- New determination of Mercury's pole position fully satisfies the equilibrium Cassini state
- New estimate of Mercury's polar moment of inertia supports the presence of a large solid inner core

Supporting Information:
- Supporting Information S1

Correspondence to:
A. Genova,
antonio.genova@uniroma1.it

Citation:
Genova, A., Goossens, S., Mazarico, E., Lemoine, F. G., Neumann, G. A., Kuang, W., et al. (2019). Geodetic evidence that Mercury has a solid inner core. *Geophysical Research Letters*, *46*, 3625–3633. https://doi.org/10.1029/2018GL081135

Received 30 OCT 2018
Accepted 10 MAR 2019
Accepted article online 15 MAR 2019
Published online 10 APR 2019

1. Introduction

Knowledge of the internal structure of the planet Mercury is fundamental to understanding its formation and evolution. The planet's high bulk density (Goettel, 1988) and weak global magnetic field (Ness et al., 1974) provided early evidence for a large central metallic core, with at least the outer part likely molten. The measurement of large-amplitude longitudinal librations confirmed the presence of a fluid outer core (Margot et al., 2007). Improved characterization of Mercury's deep interior provides crucial information on the planet's bulk composition and core cooling history.

Global exploration of Mercury was accomplished by the National Aeronautics and Space Administration's (NASA) MErcury Surface, Space ENvironment, GEochemistry, and Ranging (MESSENGER) mission (Solomon et al., 2007). The scientific payload instruments most pertinent to the planet's interior were the Mercury Laser Altimeter and the Radio Science (RS) system. Geodetic observations were acquired to determine Mercury's topography, gravitational field, rotation, and tides and to reveal details of the planet's internal structure (Zuber et al., 2012; Margot et al., 2012; Mazarico et al., 2014; Padovan et al., 2014).

A key measure of the rotational state of the planet is the mean angle ϵ between the spin axis and the normal to the orbit plane or the obliquity. This parameter, in combination with the second-degree coefficients in the spherical harmonic expansion of the planet's gravity field, gives the normalized polar moment of inertia ($\frac{C}{MR^2}$, where C, M, and R are the polar moment of inertia, mass, and radius of Mercury, respectively), which is linked to Mercury's internal mass distribution (Peale et al., 2002). Mercury's orientation model also includes the angular spin rate, which is in a 3:2 resonance with the orbital rate (Archinal et al., 2011), and its longitudinal oscillations (or forced librations) that are driven by the Sun's reversing gravitational torques on Mercury's asymmetric figure over the planet's eccentric orbit (Margot et al., 2007). Estimates of the spin rate and the amplitude of the forced physical librations in longitude (ϕ_0) provide fundamental information on the properties of Mercury's outer core and overlying silicate mantle (Peale et al., 2002). Furthermore, measurement of the gravitational potential Love number k_2 further constrains the size and rheology of these two internal regions (Padovan et al., 2014).

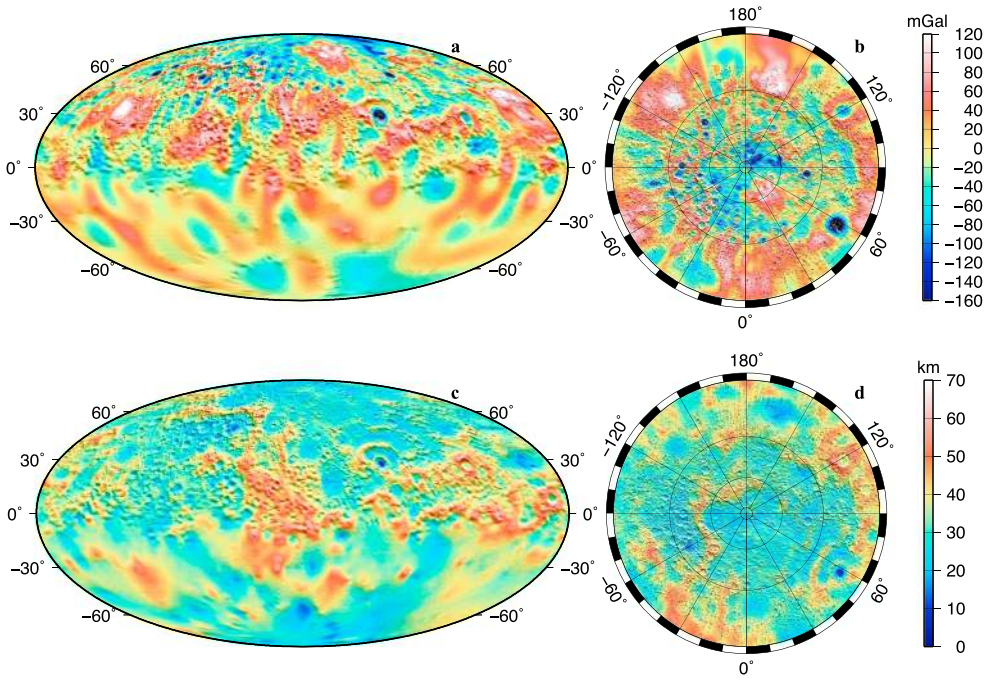

Figure 1. Maps of free-air gravity anomaly (mGal) and crustal thickness (km) on Mercury from gravity field *HgM008*, both shown over shaded topographic relief in a Mollweide projection for the entire planet (a, c) and in a polar stereographic projection for the northern hemisphere (b, d). A constant density of the crust $\rho_c = 2,800$ kg/m^3 was assumed for the calculation of crustal thickness, and the Bouguer gravity anomaly (supporting information Figure S5) was taken to be entirely the result of variations in the depth to the crust-mantle interface. An average crustal thickness of 35 km and a crust-mantle density contrast of 400 kg/m^3 were applied.

2. Methods and Geodetic Measurements

We apply a novel precision orbit determination technique (Genova et al., 2018) to the entire MESSENGER RS data set to retrieve this comprehensive set of geophysical parameters (supporting information). As part of the processing, the orbits of the spacecraft and Mercury are co-estimated and co-integrated to improve the quality of MESSENGER orbit reconstruction, a step that strongly influences the geodetic results (e.g., obliquity). This method is especially beneficial for the final year of MESSENGER RS data, which provide near-complete longitudinal coverage with lower periapsis altitude (h_p between 25 and 100 km) and lower periapsis latitude ($\phi_p < 65°$N) than earlier in the mission.

The gravitational field solution (*HgM008*) resulting from this analysis incorporates these latest data and includes substantial improvements in both short- and long-wavelength gravitational field coefficients compared with previous studies (Mazarico et al., 2014; Verma & Margot, 2016). Table S1 in the supporting information shows the enhancements in the low-degree zonal harmonic accuracies compared with the *HgM005* solution (Mazarico et al., 2014), which was retrieved before the low-altitude campaign. Refinements in the short-wavelength gravity field coefficients stand out in the maps of *HgM008* free-air gravity anomalies (Figures 1a and 1b), which reveal surface features (e.g., impact craters) in the northern hemisphere that correlate well with topography. Given a homogeneous crustal density $\rho_c = 2,800$ kg/m^3 that accounts for macroscale porosity of near-surface material similar to that observed at the Moon (Wieczorek et al., 2013) and Mars (Goossens et al., 2017), we derived Bouguer gravity anomalies that may be interpreted as variations in the depth of Mercury's crust-mantle boundary. For a crust-mantle density contrast of 400 kg/m^3 and an average crustal thickness of 35 km (supporting information), the distribution of crustal thickness is as shown in Figures 1c and 1d. The crustal thickness map was computed with finite-amplitude corrections from the gravitational and topographic fields in the spherical harmonic degree range 2 to 60 (Wieczorek, 2015).

To investigate Mercury's mantle and core structure, the *HgM008* gravity field solution also includes adjustments to Mercury's orientation model and gravitational tide. Our precision orbit determination methodology

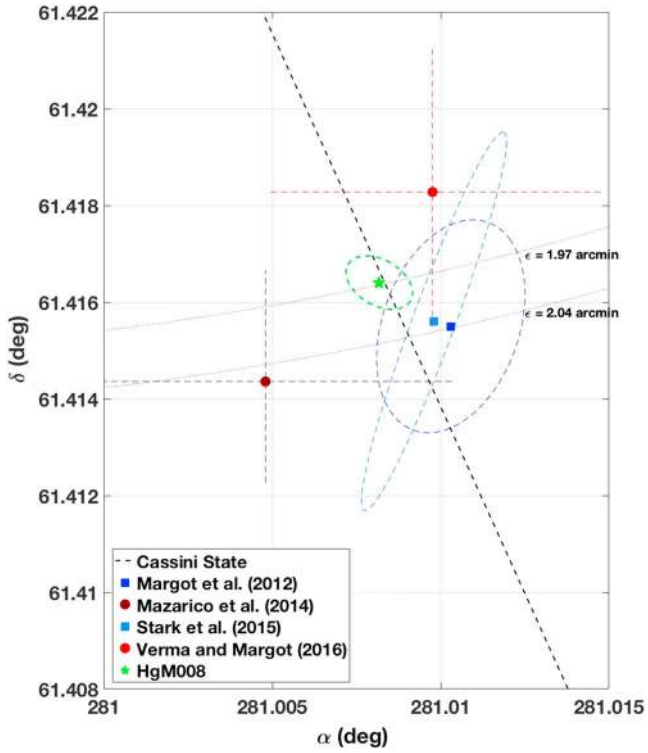

Figure 2. Right ascension (α) and declination (δ) of the pole in the International Celestial Reference Frame at the epoch J2000. The orientation of Mercury's spin axis was earlier determined from Earth-based radar measurements (Margot et al., 2012), a combination of altimeter and imaging data (Stark et al., 2015), and gravity (Mazarico et al., 2014; Verma & Margot, 2016). Our latest solution ($\alpha = 281.0082° \pm 0.0009°$, $\delta = 61.4164° \pm 0.0003°$), which follows closely the Cassini state (black dashed line), shows a more precise measurement of the planet's orientation than those from previous gravity solutions. Mazarico et al. (2014) and Verma and Margot (2016) reported only the formal uncertainties of the right ascension and declination of the pole scaled by 10 (red dashed lines). The uncertainties in the Margot et al. (2012), Stark et al. (2015), and *HgM008* solutions are shown as 95% confidence error ellipses that account for the correlation between α and δ.

enables us to retrieve both spin and orbital rates and thus directly estimate a possible departure from the 3:2 spin-orbit resonance. We find that the spin rate is 2.7×10^{-6}°/day larger than the equilibrium state associated with the 3:2 spin-orbit resonance (supporting information). This result may provide information on the mechanisms that led Mercury to its current minimum energy condition, possibly including core-mantle friction (Correia & Laskar, 2004) or an impact event sufficiently large to perturb earlier spin-orbit synchronicity (Wieczorek et al., 2012).

Constraints on the present state of the mantle can be obtained from the gravitational tide. The gravitational potential Love number k_2 in the *HgM008* solution is 0.5690 ± 0.025 (the uncertainty encompasses variations among different solutions rather than only statistical error), which is larger than previous estimates (Mazarico et al., 2014; Verma & Margot, 2016) by ~0.1. Inclusion of data from the final year of the MESSENGER mission is the main source of this significant difference. The low-altitude campaign enabled the acquisition of gravity measurements at high latitudes and 25- to 100-km altitudes, leading to a better understanding of the planet's tidal response. A larger k_2 indicates a warm and weak mantle rather than a cold and rigid mantle or the presence of a solid Fe-S layer at the top of the core, as suggested previously (Hauck et al., 2013; Padovan et al., 2014). A solid Fe-S layer denser than the overlying mantle was initially hypothesized to fit early gravity and orientation measurements and was motivated in part by the chemically reduced state of Mercury's surface materials (Hauck et al., 2013). An improved estimate of Mercury's obliquity (Margot et al., 2012) removed the requirement for a high-density layer such as Fe-S at the base of the mantle or top of the core but still allowed such a layer (Knibbe & van Westrenen, 2015).

The measured value of k_2 supports the presence of a molten core, which is responsible for the decoupling between the outer silicate shell and the fluid core at short timescales (e.g., ~88 days), leading to a large

amplitude of the longitudinal libration. Our measurement of libration amplitude, $\phi_0 = 40.0 \pm 8.7$ arcsec (3 standard deviations), is consistent with the results presented by Margot et al. (2007, 2012) and Stark et al. (2015). These studies provided direct measurements of surface motions and are still the most accurate estimates of the amplitude of the physical librations in longitude. Our gravity measurement of the forced librations is sensitive to both the interior structure and the surface shape and carries larger uncertainties.

The coestimation of the rotational model with the gravity field provides the mean orientation of the distinct shells that make up Mercury's internal structure. This measurement methodology is well suited to retrieve information on the deeper interior that is not detectable from observations only of the surface. The definition of the normalized polar moment of inertia $\frac{C}{MR^2}$ of the entire planet is based on the assumption that dissipative processes maintain Mercury in the equilibrium Cassini state, in which the spin axis, orbit precession axis, and orbit-plane normal are coplanar (Peale et al., 2002). The spin pole orientation recovered from Earth-based radar measurements (Margot et al., 2012) and MESSENGER altimetric and imaging data (Stark et al., 2015) showed a substantial offset from the Cassini state and led to a normalized polar moment of inertia $\frac{C}{MR^2}$ of 0.346–0.353, a range that suggests a relatively low level of interior differentiation. In contrast, our estimation of the planet's orientation yields an average obliquity for the whole planet that is in full agreement with the Cassini state.

This result is illustrated in Figure 2, which shows the right ascension (α) and declination (δ) of different spin pole solutions, reported in the International Celestial Reference Frame at the reference epoch J2000. Our *HgM008* solution, $\alpha = 281.0082° \pm 0.0009°$ (3 standard deviations), $\delta = 61.4164° \pm 0.0003°$ (3 standard deviations), stands out from those of previous gravity investigations (Mazarico et al., 2014; Verma & Margot, 2016) and is in close agreement with the Cassini state (Peale, 1988; Baland et al., 2017), even in the absence of any constraint on α and δ. The HgM008 pole orientation differs significantly from the estimates by Margot et al. (2012) and Stark et al. (2015), since its central value is not within the 95% confidence (∼3 standard deviations) error ellipses of either earlier study (Figure 2). Both of those groups analyzed the positions of features on Mercury's surface, and the solutions may therefore be representative only of the orientation state of Mercury's outer solid shell (crust and mantle), because the fluid core is mechanically decoupled (Margot et al., 2007). Our measurement of $\epsilon = 1.968 \pm 0.027$ arcmin (3 standard deviations) is only ∼ 3.5% (3.6–4.3 arcsec) less than the two estimates derived from surface features, but this small change and the higher precision in the pole's orientation add new confidence to the computation of the polar moment of inertia of the entire planet by confirming that Mercury's orientation is in the equilibrium Cassini state. Our measured obliquity yields $\frac{C}{MR^2} = 0.333 \pm 0.005$ (the uncertainty is computed by assuming 3 standard deviation values for our measured quantities and is thus more conservative than if we were to use 1 standard deviation values). This result suggests a more differentiated interior structure than did the previous estimate of 0.346 ± 0.014 (Margot et al., 2012), a value that provided only limited information on Mercury's deep interior (Hauck et al., 2013). Our lower value for the polar moment of inertia and an uncertainty reduced by a factor of 3 (notwithstanding our conservative use of 3 standard deviation values) compared with previous estimates hints at a solid inner core having a higher density than the fluid outer core. The presence of a large solid inner core could also be confirmed by a reduced amplitude of the longitudinal librations (Van Hoolst et al., 2012). However, the current uncertainty in ϕ_0 is still too large to detect these effects, which lead to a reduction of the libration amplitude by up to ∼20 m for a nearly fully solidified core.

A difference between the obliquity value derived from gravity information and that from surface measurements also is consistent with the presence of a solid inner core. The spin axis of Mercury's outer solid shell tends to be forced toward the Cassini state by the strong pressure torque between the outer molten core and the mantle. An additional gravitational torque on that shell may be generated by a solid inner core that departs from spherical symmetry (Peale et al., 2016). This mechanism could be responsible for the difference between the obliquity measured from surface features and the Cassini state.

The fractional polar moment of inertia of the solid crust plus mantle ($C_{\mathrm{cr+m}}$) provides an additional constraint on models of the interior. Peale et al. (2002) formulated a method to estimate the ratio $\frac{C_{\mathrm{cr+m}}}{C}$ from the combined measurements of the planet's obliquity, the amplitude of the longitudinal librations (ϕ_0), and the second-degree gravity field. The gravity field and spin measurements from surface features provide the most accurate estimates of the obliquity and forced librations, respectively. With our measured value of ϵ and the Margot et al. (2012) estimate of ϕ_0, we compute $\frac{C_{\mathrm{cr+m}}}{C} = 0.443 \pm 0.019$ (as with the uncertainty on $\frac{C}{MR^2}$, the uncertainty here is derived from 3 standard deviation uncertainties in our measured ϵ and the Margot et al. (2012) value for ϕ_0).

3. Interior Modeling Results

Our measurements of the dimensionless polar moments of inertia $\frac{C}{MR^2}$ and $\frac{C_{cr+m}}{C}$, together with the bulk density of the planet inferred from Mercury's $GM = 22031.8636 \pm 0.006 \times 10^9$ m^3/s^2, where G is the gravitational constant, enable a quantitative exploration of the properties of Mercury's interior structure, particularly the size of an inner core. The scope of our interior modeling investigation is focused on the influence of the new moment of inertia value on the properties of Mercury's deep interior. For this reason, we did not include in our internal model determination the Love number k_2, which provides information more sensitive to the outer silicate layers than the solid inner core (Padovan et al., 2014). Knowledge of k_2 and the radial displacement Love number h_2, the latter of which is still unknown in value, may enable a better characterization of the deep interior (Steinbrügge et al., 2018). We adapted a Markov chain Monte Carlo (MCMC) algorithm to generate ensembles of interior models that satisfy these geophysical constraints. The uncertainties for $\tilde{C} = \frac{C}{MR^2}$, $\tilde{C}_{\mathrm{cr+m}} = \frac{C_{\mathrm{cr+m}}}{C}$, and the bulk density ρ adopted in the MCMC probability function are $\sigma_{\tilde{C}} = 0.005$, $\sigma_{\tilde{C}_{\mathrm{cr+m}}} = 0.019$, and $\sigma_\rho = 0.002\rho$ (supporting information). The uncertainty in ρ accounts mainly for possible inaccuracies in the shape of Mercury (Perry et al., 2015). The uncertainties in both $\tilde{C}$ and $\tilde{C}_{\mathrm{cr+m}}$ represent conservative values because we used the 3 standard deviation value for the obliquity when deriving the associated errors for these quantities. Because of these conservative uncertainties in the measurements, the associated uncertainties in the parameters determined with our MCMC method will be affected accordingly and thus do not require additional scale factors.

The methods implemented in this study may be divided into two cases. First, we consider a four-shell planet (inner core, outer core, mantle, and crust), with the only assumption that the density (constant within each shell) increases with depth (supporting information). The second (multilayer) approach includes four (or five) shells in the interior, but for this approach we divide each shell further into 1-km-thick sublayers, to account for the effects of pressure on density and gravitational acceleration (Hauck et al., 2013; Knibbe & van Westrenen, 2015), and we solve the equation of state (EoS) in the mantle and the core.

The four-shell constant-density approach enables a better mapping of the parameter space. Each shell has an outer radius and a uniform density that are both adjusted in the MCMC algorithm. Table S2 in the supporting information shows the boundary conditions of these estimated parameters, including the constraints that the shell outer radius and density decrease and increase with depth, respectively.

The multilayer approach permits incorporation of internally consistent profiles of pressure, temperature, and density. However, the crust is modeled as a constant-density layer and its thickness and density are adjusted parameters. Our multilayer results were retrieved with two different methodologies for modeling the mantle. First, we considered the mantle as a constant-density layer to account for conservative bounds on the structure of the silicate shells in a manner similar to the four-shell case. The second method includes an EoS for the mantle, the parameters of which are listed in Table S4 of the supporting information. The MCMC multilayer results are insensitive to whether the mantle is modeled as a constant-density layer or with an appropriate EoS. In contrast, the variation of density with depth and, therefore, the effects of compression are fundamental in the inner core and outer core, and their composition must be assumed to solve the EoS.

We studied four distinct scenarios under which sulfur (S) or silicon (Si) serves as the principal light element that is alloyed with iron in the core (supporting information). Sulfur has a substantial affinity for Fe, and its presence on the surface of Mercury, as measured by MESSENGER's X-Ray Spectrometer (XRS) (Nittler et al., 2011), suggests that an Fe-S composition may be responsible for the fluid state of the outer molten core. Silicon, an abundant element on Mercury's surface, is more soluble in molten Fe under the chemically reducing conditions found for Mercury surface materials and inferred to characterize the interior (Hauck et al., 2013). The scenarios investigated in this study include the following: Fe-S models with a variable percentage of sulfur (0–25%) in the outer core and an inner core of pure iron (*Fe-S case*), Fe-S models otherwise similar but with a solid Fe_3S layer overlying the inner core (Fe_3S case), Fe-Si models with the same weight fraction for Si (0–25%) in both the inner core and outer core (Fe-Si case), and models featuring a fluid outer core with two distinct layers of molten Fe-Si and Fe-S alloys and a solid Fe-S layer at the top of the core (Fe-S-Si case). This latter compositional model is an end-member that explicitly invokes liquid-liquid immiscibility in the Fe-S-Si system at Mercury's outer core pressures and the likelihood that the Fe-S and Fe-Si alloys have segregated as a result of their distinct densities (Hauck et al., 2013; Knibbe & van Westrenen, 2015).

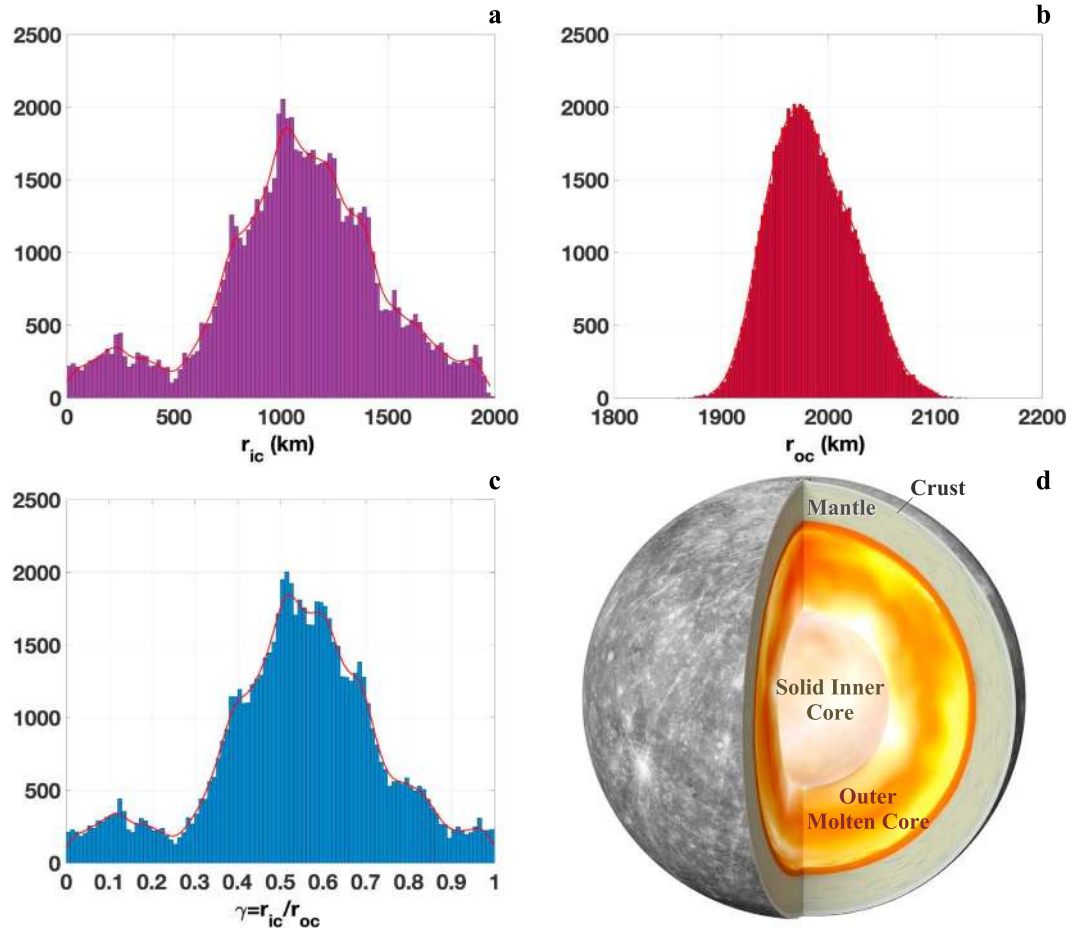

Figure 3. Histograms of the (a) inner core radius, r_{ic}, (b) outer core radius, r_{oc}, and (c) their ratio γ for the samples of four-shell Markov chain Monte Carlo solutions. The multilayer Markov chain Monte Carlo solutions, which account for the effects of compression in the inner core and outer core, are reported in the supporting information. (d) Schematic cutaway view of Mercury's interior structure.

The multilayer solutions show a strong dependence on assumed model composition. For the Fe-S and Fe-Si scenarios, the ensembles satisfy the moment of inertia constraints. The former set, in particular, provides an ensemble of solutions that are in agreement with both $\frac{C}{MR^2}$ and $\frac{C_{cr+m}}{C}$. The other two cases, Fe_3S and Fe-S-Si, do not fully converge to the measured moments of inertia (supporting information). The four-shell constant-density model can also satisfy the $\frac{C}{MR^2}$ and $\frac{C_{cr+m}}{C}$ constraints.

Under both the four-shell constant-density and multilayer MCMC approaches, we perturbed a set of parameters to investigate a broad range of possible interior structures (supporting information). These model parameters are reported in Tables S2 and S3 for the four-shell constant-density and multilayer MCMC approaches, respectively. The probability distributions of the parameters of interest were explored by means of random walkers. Among the model parameters perturbed were the inner core (r_{ic}) and outer (r_{oc}) core radii, which were derived with the sole constraint that $0 < r_{ic} < r_{oc}$.

In each case, the parameter that is best determined (because its a posteriori distribution closely follows a Gaussian distribution with a narrow standard deviation) is r_{oc}. The four-shell and multilayer cases provide consistent estimates of the outer core radius. A value of $r_{oc} = 1985 \pm 39$ km, with the uncertainty computed from 1 standard deviation value of the ensemble distribution, was determined in the four-shell case (Figure 3b). The multilayer solution with an Fe-Si alloy in the outer core and inner core converged to $r_{oc} = 1967 \pm 23$ km (Figure S7D), which is significantly lower than results of previous studies that were based on an obliquity of the spin axis derived from tracking of surface features (Hauck et al., 2013).

The retrieved ratio $\gamma = \frac{r_{ic}}{r_{oc}}$ of inner core radius to outer core radius for ensembles obtained with the MCMC four-shell constant-density models and the multilayer models is shown in Figures 3c and S8. These solutions suggest the presence of a large solid inner core. The ensemble average $\frac{r_{ic}}{r_{oc}}$ ratios are 0.538 ± 0.195 and 0.445 ± 0.181 (the uncertainties are 1 standard deviation values of the ensemble distributions) for the MCMC four-shell constant-density and multilayer Fe-Si cases, respectively. The multilayer cases with an Fe-S outer core and a pure-Fe inner core also provide evidence for the presence of a solid inner core with a radius ≥ 0.4 r_{oc}. Neither the Fe-S nor the Fe-Si cases consider the possible incorporation of other elements into the core, for example, S for Fe-Si cases, Si for Fe-S cases, or Ni for both cases (Chabot et al., 2014). The equations of state for such multicomponent systems are not well known, however, and thus, we investigated only cases with layers composed of binary mixtures of Fe and lighter elements that have been studied in earlier analyses (Hauck et al., 2013; Knibbe & van Westrenen, 2015).

4. Conclusions

On the basis of our geophysical results and modeling, we are able to retrieve important properties of Mercury's interior, including a high-resolution crustal thickness map and new constraints on the size of the solid inner core (Figure 3b). Our measurements of the normalized polar moments of inertia ($\frac{C}{MR^2}$, $\frac{C_{cr+m}}{C}$) provide an inner core radius ratio $\gamma = 0.445 \pm 0.181$ for an Fe-Si alloy in both the outer core and inner core and a ratio $\gamma = 0.517 \pm 0.170$ for an Fe-S-Si core. Although the uncertainties in γ given here are the standard deviation of the ensemble distributions, they represent conservative values because for our MCMC method we adopted 3 standard deviation uncertainties for our measured obliquity ϵ to determine the uncertainties in the normalized polar moments of inertia. Additional insight into the structure of Mercury's core can be expected from the exploration of magnetic dynamo models that match the characteristics of Mercury's internal magnetic field (Cao et al., 2014; Tian et al., 2015).

Acknowledgments
We thank the MESSENGER operations and engineering teams for enabling the collection of radio science data during the mission's low-altitude campaign. We are also grateful to J. B. Nicholas (EST, Inc.), D. E. Pavlis (University of Maryland/Earth System Science Interdisciplinary Center, ESSIC), and D. D. Rowlands (NASA Goddard Space Flight Center) for their help with the GEODYN II software. We thank Jurrien Knibbe and an anonymous reviewer for their constructive comments on an earlier draft of this paper. The data used in this paper are available on the Geosciences Node of the NASA Planetary Data System at their website (http://pds-geosciences.wustl.edu/messenger/mess-v_h-rss-1-edr-rawdata-v1/messrs_0xxx/). The gravity field solution *HgM008*, which includes the spherical harmonic coefficients, their associated uncertainties, and the full covariance matrix, is available on the NASA GSFC portal at their website (https://pgda.gsfc.nasa.gov) and on the Geosciences Node of NASA Planetary Data System at their website (http://pds-geosciences.wustl.edu/messenger/mess-h-rss_mla-5-sdp-v1/messrs_1001/).

References

Archinal, B. A., A'Hearn, M. F., Bowell, E., Conrad, A., Consolmagno, G. J., Courtin, R., et al. (2011). Report of the IAU Working Group on Cartographic Coordinates and Rotational Elements: 2009. *Celestial Mechanics and Dynamical Astronomy*, *109*(2), 101–135.

Baland, R.-M., Yseboodt, M., Rivoldini, A., & Van Hoolst, T. (2017). Obliquity of Mercury: Influence of the precession of the pericenter and of tides. *Icarus*, *291*(1), 136–159.

Cao, H., Aurnou, J. M., Wicht, J., Dietrich, W., Soderlund, K. M., & Russell, C. T. (2014). A dynamo explanation for Mercury's anomalous magnetic field. *Geophysical Research Letters*, *41*, 4127–4134. https://doi.org/10.1002/2014GL060196

Chabot, N. L., Wollack, E. A., Klima, R. L., & Minitti, M. E. (2014). Experimental constraints on Mercury's core composition. *Earth and Planetary Science Letters*, *390*(1), 199–208.

Correia, A. C., & Laskar, J. (2004). Mercury's capture into the 3/2 spin-orbit resonance as a result of its chaotic dynamics. *Nature*, *429*(6994), 848–850.

Genova, A., Mazarico, E., Goossens, S., Lemoine, F. G., Neumann, G. A., Smith, D. E., & Zuber, M. T. (2018). Solar system expansion and strong equivalence principle as seen by the NASA MESSENGER mission. *Nature Communications*, *9*(1), 289.

Goettel, K. A. (1988). Present bounds on the bulk composition of Mercury: Implications for planetary formation processes. In F. Vilas, C. R. Chapman, & M. S. Matthews (Eds.), *Mercury* pp. 613–621). Tucson, AZ: Univ. Arizona Press.

Goossens, S., Sabaka, T. J., Genova, A., Mazarico, E., Nicholas, J. B., & Neumann, G. A. (2017). Evidence for a low bulk crustal density for Mars from gravity and topography. *Geophysical Research Letters*, *44*, 7686–7694. https://doi.org/10.1002/2017GL074172

Hauck, S. A. II, Margot, J.-L., Solomon, S. C., Phillips, R. J., Johnson, C. L., Lemoine, F. G., et al. (2013). The curious case of Mercury's internal structure. *Journal of Geophysical Research: Planets*, *118*, 1204–1220. https://doi.org/10.1002/jgre.20091

Knibbe, J., & van Westrenen, W. (2015). The interior configuration of planet Mercury constrained by moment of inertia and planetary contraction. *Journal of Geophysical Research: Planets*, *120*, 1904–1923. https://doi.org/10.1002/2015JE004908

Margot, J.-L., Peale, S., Jurgens, R., Slade, M., & Holin, I. (2007). Large longitude libration of Mercury reveals a molten core. *Science*, *316*(5825), 710–714.

Margot, J.-L., Peale, S. J., Solomon, S. C., Hauck, S. A. II, Ghigo, F. D., Jurgens, R. F., et al. (2012). Mercury's moment of inertia from spin and gravity data. *Journal of Geophysical Research*, *117*, E00L09. https://doi.org/10.1029/2012JE004161

Mazarico, E., Genova, A., Goossens, S., Lemoine, F. G., Neumann, G. A., Zuber, M. T., et al. (2014). The gravity field, orientation, and ephemeris of Mercury from MESSENGER observations after three years in orbit. *Journal of Geophysical Research: Planets*, *119*, 2417–2436. https://doi.org/10.1002/2014JE004675

Ness, N., Behannon, K., Lepping, R., Whang, Y., & Schatten, K. (1974). Magnetic field observations near Mercury: Preliminary results from Mariner 10. *Science*, *185*(4146), 151–160.

Nittler, L. R., Starr, R. D., Weider, S. Z., McCoy, T. J., Boynton, W. V., Ebel, D. S., et al. (2011). The major-element composition of Mercury's surface from MESSENGER X-ray spectrometry. *Science*, *333*(6051), 1847–1850.

Padovan, S., Margot, J.-L., Hauck, S. A. II, Moore, W. B., & Solomon, S. C. (2014). The tides of Mercury and possible implications for its interior structure. *Journal of Geophysical Research: Planets*, *119*, 850–866. https://doi.org/10.1002/2013JE004459

Peale, S. J. (1988). The rotational dynamics of Mercury and the state of its core. In F. Vilas, C. R. Chapman, & M. S. Matthews (Eds.), *Mercury* pp. 461–493). Tucson, AZ: Univ. Arizona Press.

Peale, S. J., Margot, J.-L., Hauck, S. A. II, & Solomon, S. C. (2016). Consequences of a solid inner core on Mercury's spin configuration. *Icarus*, *264*(1), 443–455.

Peale, S. J., Phillips, R. J., Solomon, S. C., Smith, D. E., & Zuber, M. T. (2002). A procedure for determining the nature of Mercury's core. *Meteoritics & Planetary Science*, *37*(9), 1269–1283.
Perry, M. E., Neumann, G. A., Phillips, R. J., Barnouin, O. S., Ernst, C. M., Kahan, D. S., et al. (2015). The low-degree shape of Mercury. *Geophysical Research Letters*, *42*, 6951–6958. https://doi.org/10.1002/2015GL065101
Solomon, S. C., McNutt, R. L. Jr., Gold, R. E., & Domingue, D. L. (2007). MESSENGER mission overview. *Space Science Reviews*, *131*(1-4), 3–39.
Stark, A., Oberst, J., Preusker, F., Peale, S. J., Margot, J.-L., Phillips, R. J., et al. (2015). First MESSENGER orbital observations of Mercury's librations. *Geophysical Research Letters*, *42*, 7881–7889. https://doi.org/10.1002/2015GL065152
Steinbrügge, G., Padovan, S., Hussmann, H., Steinke, T., Stark, A., & Oberst, J. (2018). Viscoelastic tides of Mercury and the determination of its inner core size. *Journal of Geophysical Research: Planets*, *123*, 2760–2772. https://doi.org/10.1029/2018JE005569
Tian, Z., Zuber, M. T., & Stanley, S. (2015). Magnetic field modeling for Mercury using dynamo models with a stable layer and laterally variable heat flux. *Icarus*, *260*, 263–268.
Van Hoolst, T., Rivoldini, A., Baland, R.-M., & Yseboodt, M. (2012). The effect of tides and an inner core on the forced longitudinal libration of Mercury. *Earth and Planetary Science Letters*, *333*, 83–90.
Verma, A. K., & Margot, J.-L. (2016). Mercury's gravity, tides, and spin from MESSENGER radio science data. *Journal of Geophysical Research: Planets*, *121*, 1627–1640. https://doi.org/10.1002/2016JE005037
Wieczorek, M. A., Correia, A. C. M., Le Feuvre, M., Laskar, J., & Rambaux, N. (2012). Mercury's spin-orbit resonance explained by initial retrograde and subsequent synchronous rotation. *Nature Geoscience*, *5*(1), 18–21.
Wieczorek, M. A., Neumann, G. A., Nimmo, F., Kiefer, W. S., Taylor, G. J., Melosh, H. J., et al. (2013). The crust of the Moon as seen by GRAIL. *Science*, *339*(6120), 671–675.
Wieczorek, M. A., & Phillips, R. J. (1998). Potential anomalies on a sphere: Applications to the thickness of the lunar crust. *Journal of Geophysical Research*, *103*(E1), 1715–1724.
Zuber, M. T., Smith, D. E., Phillips, R. J., Solomon, S. C., Neumann, G. A., Hauck, S. A. II, et al. (2012). Topography of the northern hemisphere of Mercury from MESSENGER laser altimetry. *Science*, *336*(6078), 217–220.

References From the Supporting Information

Anderson, W. W., & Ahrens, T. J. (1994). An equation of state for liquid iron and implications for the Earth's core. *Journal of Geophysical Research*, *99*(B3), 4273–4284.
Balog, P., Secco, R., Rubie, D., & Frost, D. (2003). Equation of state of liquid Fe-10 wt% S: Implications for the metallic cores of planetary bodies. *Journal of Geophysical Research*, *108*(B2), 2124. https://doi.org/10.1029/2001JB001646
Breuer, D., Rueckriemen, T., & Spohn, T. (2015). Iron snow, crystal floats, and inner-core growth: Modes of core solidification and implications for dynamos in terrestrial planets and moons. *Progress in Earth and Planetary Science*, *2*(39), 1–26.
Colombo, G., & Shapiro, I. I. (1966). The rotation of the planet Mercury. *The Astrophysical Journal*, *145*(1), 296–307.
Davies, M. E., Abalakin, V. K., Cross, C. A., Duncombe, R. L., Masursky, H., Morando, B., et al. (1980). Report of the IAU Working Group on Cartographic Coordinates and Rotational Elements of the planets and satellites. *Celestial Mechanics and Dynamical Astronomy*, *22*(3), 205–230.
Fei, Y., Li, J., Bertka, C. M., & Prewitt, C. T. (2000). Structure type and bulk modulus of Fe3S, a new iron-sulfur compound. *American Mineralogist*, *85*(11-12), 1830–1833.
Folkner, W. M. (2014). Planetary Ephemeris DE432 (*Memorandum IOM 392R-14-003*). Pasadena, CA: Jet Propulsion Laboratory, California Institute of Technology.
Foreman-Mackey, D., Hogg, D. W., Lang, D., & Goodman, J. (2016). emcee: The MCMC Hammer. *Publications of the Astronomical Society of the Pacific*, *125*(2), 306–312.
Harder, H., & Schubert, G. (2001). Sulfur in Mercury's core? *Icarus*, *151*(1), 118–122.
Hastings, W. K. (1970). Monte Carlo sampling methods using Markov chains and their applications. *Biometrika*, *57*(1), 97–109.
Hauck, S. A. II, Solomon, S. C., & Smith, D. A. (2007). Predicted recovery of Mercury's internal structure by MESSENGER. *Geophysical Research Letters*, *34*, L18201. https://doi.org/10.1029/2007GL030793
James, P. B., Zuber, M. T., Phillips, R. J., & Solomon, S. C. (2015). Support of long-wavelength topography on Mercury inferred from MESSENGER measurements of gravity and topography. *Journal of Geophysical Research: Planets*, *120*, 287–310. https://doi.org/10.1002/2014JE004713
Jing, Z., Wang, Y., Kono, Y., Yu, T., Sakamaki, T., Park, C., et al. (2014). Sound velocity of Fe-S liquids at high pressure: Implications for the Moon's molten outer core. *Earth and Planetary Science Letters*, *396*(1), 78–87.
Kaula, W. M. (2013). *Theory of satellite geodesy: Applications of satellites to geodesy*. Mineola, NY: Dover Publications.
Khan, A., Connolly, J. A. D., Maclennan, J., & Mosegaard, K. (2007). Joint inversion of seismic and gravity data for lunar composition and thermal state. *Geophysical Journal International*, *168*(1), 243–258. https://doi.org/10.1111/j.1365-246X.2006.03200.x
Khan, A., Connolly, J., Pommier, A., & Noir, J. (2014). Geophysical evidence for melt in the deep lunar interior and implications for lunar evolution. *Journal of Geophysical Research: Planets*, *119*, 2197–2221. https://doi.org/10.1002/2014JE004661
Khan, A., Liebske, C., Rozel, A., Rivoldini, A., Nimmo, F., Connolly, J., et al. (2018). A geophysical perspective on the bulk composition of Mars. *Journal of Geophysical Research: Planets*, *123*, 575–611. https://doi.org/10.1002/2017JE005371
Klaasen, K. P. (1976). Mercury's rotation axis and period. *Icarus*, *28*(4), 469–478.
Komabayashi, T., & Fei, Y. (2010). Internally consistent thermodynamic database for iron to the Earth's core conditions. *Journal of Geophysical Research*, *115*, B03202. https://doi.org/10.1029/2009JB006442
Konopliv, A., Banerdt, W., & Sjogren, W. (1999). Venus gravity: 180th degree and order model. *Icarus*, *139*(1), 3–18.
Lin, J.-F., Campbell, A. J., Heinz, D. L., & Shen, G. (2003). Static compression of iron–silicon alloys: Implications for silicon in the Earth's core. *Journal of Geophysical Research*, *108*(B1), 2045. https://doi.org/10.1029/2002JB001978
Margot, J.-L. (2009). A Mercury orientation model including non-zero obliquity and librations. *Celestial Mechanics and Dynamical Astronomy*, *105*(4), 329–336.
Matsumoto, K., Yamada, R., Kikuchi, F., Kamata, S., Ishihara, Y., Iwata, T., et al. (2015). Internal structure of the Moon inferred from Apollo seismic data and selenodetic data from GRAIL and LLR. *Geophysical Research Letters*, *42*, 7351–7358. https://doi.org/10.1002/2015GL065335
Matsuyama, I., Nimmo, F., Keane, J. T., Chan, N. H., Taylor, G., Wieczorek, M. A., et al. (2016). GRAIL, LLR, and LOLA constraints on the interior structure of the Moon. *Geophysical Research Letters*, *43*, 8365–8375. https://doi.org/10.1002/2016GL069952

Metropolis, N., Rosenbluth, A. W., Rosenbluth, M. N., Teller, A. H., & Teller, E. (1953). Equation of state calculations by fast computing machines. *The Journal of Chemical Physics*, *21*(6), 1087–1092.

More, J., Sorenson, D., Garbow, B., & Hillstrom, K. (1984). The MINPACK Project. In W. Cowell (Ed.), *Sources and development of mathematical software* pp. 88–111). Upper Saddle River, NJ: Prentice-Hall.

Mosegaard, K., & Tarantola, A. (1995). Monte Carlo sampling of solutions to inverse problems. *Journal of Geophysical Research*, *100*(B7), 12,431–12,447. https://doi.org/10.1029/94JB03097

Padovan, S., Wieczorek, M. A., Margot, J.-L., Tosi, N., & Solomon, S. C. (2015). Thickness of the crust of Mercury from geoid-to-topography ratios. *Geophysical Research Letters*, *42*, 1029–1038. https://doi.org/10.1002/2014GL062487

Pavlis, D. E., Wimert, J., & McCarthy, J. J. (2013). *GEODYN II System Description*, vol. 1-5. Greenbelt, MD: SGT Inc.

Pettengill, G. H., & Dyce, R. B. (1965). A radar determination of the rotation of the planet Mercury. *Nature*, *206*(4990), 1240–1240.

Rivoldini, A., Van Hoolst, T., Verhoeven, O., Mocquet, A., & Dehant, V. (2011). Geodesy constraints on the interior structure and composition of Mars. *Icarus*, *213*(2), 451–472. https://doi.org/10.1016/j.icarus.2011.03.024

Sanloup, C., Fiquet, G., Gregoryanz, E., Morard, G., & Mezouar, M. (2004). Effect of Si on liquid Fe compressibility: Implications for sound velocity in core materials. *Geophysical Research Letters*, *31*, L07604. https://doi.org/10.1029/2004GL019526

Sanloup, C., Guyot, F., Gillet, P., Fiquet, G., Mezouar, M., & Martinez, I. (2000). Density measurements of liquid Fe-S alloys at high-pressure. *Geophysical Research Letters*, *27*(6), 811–814.

Srinivasan, D. K., Perry, M. E., Fielhauer, K. B., Smith, D. E., & Zuber, M. T. (2007). The radio frequency subsystem and radio science on the MESSENGER mission. *Space Science Reviews*, *131*(1), 557–571.

Stockstill-Cahill, K. R., McCoy, T. J., Nittler, L. R., Weider, S. Z., & Hauck, S. A. II (2012). Magnesium-rich crustal compositions on Mercury: Implications for magmatism from petrologic modeling. *Journal of Geophysical Research*, *117*, E00L15. https://doi.org/10.1029/2012JE004140

Wieczorek, M. A. (2015). Gravity and topography of the terrestrial planets. In T. Spohn (Ed.), *Planets and Moons*, Vol. 10 in Treatise on Geophysics, G. Schubert (Ed.) (pp. 153–193). Oxford, UK: Elsevier.

Yseboodt, M., & Margot, J.-L. (2006). Evolution of Mercury's obliquity. *Icarus*, *181*(2), 327–337.

Yu, X., & Secco, R. A. (2008). Equation of state of liquid Fe-17 wt% Si to 12 GPa. *High Pressure Research*, *28*(1), 19–28.